Nano Research

Open Access

Research Article

B-doped carbon nanotubes for enhanced adsorption of NO_3^- and promoted electrocatalysis on transformation nitrate into ammonia

Ce Zhou, Yaoting Huang, Chenqi Liu, Chenxi Wang, Wenjing Fang, Hong Xia, Yibing Song, Muwei Ji ✉, and Fushen Lu ✉

Key (Guangdong-Hong Kong Joint) Laboratory for Preparation and Application of Ordered Structural Materials of Guangdong Province, Guangdong Engineering Technology Research Center of Advanced Polymer Synthesis, College of Chemistry and Chemical Engineering, Shantou University, Shantou 515063, China

Cite this article: *Nano Research*, **2026**, *19*, 94908512. https://doi.org/10.26599/NR.2026.94908512

ABSTRACT: Electronic nitrate reduction reaction (NO_3RR) is an expected process to obtain green ammonia and bring a hot topic on electrocatalyst constructing. Nevertheless, NO_3RR processes a complex path with multiple adsorption and desorption so that the adsorbed selectivity is one of the key points. Herein, based on the catalysis of Cu_2O-Fe_3O_4 on N-doped carbon nanotubes (NCNTs), B-doped sites were introduced for enhancing the adsorption of NO_3^- and thereby increasing the local concentration on surface of the electrode. After confirming the catalytic sites mainly from Cu_2O and Fe_3O_4 nanoparticles, the B,N-doped carbon nanotube (BNCNT) substrate was discovered accelerating the NO_3RR with high yield NH_3 and positive-shift of onset potential. The enhancement from B-sites was also testified by the performance comparison using different substrate and series of metal oxide/BNCNTs, presenting the general strategy for promoting NO_3RR. This work provides a new perspective for modulating catalytic process, especially in the complex electrocatalysis with high-required selectivity and concentration-dependence.

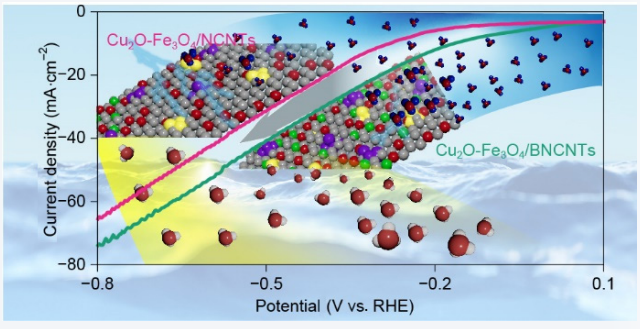

KEYWORDS: B-doped nitrate reduction reaction, adsorption enhancements of nitrate, nitrate reduction, ammonia production

1 Introduction

Ammonia is the cornerstone of modern agriculture and industry, serving as the primary nitrogen source for global food production and the key raw material for many industrial chemicals [1, 2]. Compared with the traditional Haber–Bosch method of industrial ammonia synthesis [3], electrocatalytic nitrate reduction (NO_3RR) offer a mild method of ammonia synthesis [4–6], reducing the requirements of reaction conditions and mitigating subsequent pollutant nitrate pollution [5, 7, 8]. By coupling with special electronic oxidation reaction, NO_3RR holds a great potential for industrial valuable products [9]. Furthermore, in the NO_3RR process, some active species generate for C–N coupling to produce chemical compounds with high values, offering the advantages over traditional methods [10]. However, th electrocatalytic synthesis of ammonia also faces great challenges [11, 12], involving the transfer of 8 electrons and 9 protons and generating multiple intermediate products [13, 14]. Hence, NO_3RR is considered extremely unfavorable to improve the selectivity of ammonia reduction and the corresponding Faradaic efficiency [15]. To address the issue, many kinds of catalysts were explored via the modulation electronic structure of catalytic sites, enhancing the tandem reaction coupling [16–21]. Cobalt single-atom (I-CoN_4) catalyst was modified a second iodine-doped shell via a mild etching synchronous doping strategy and enabled the construction of tandem catalytic sites with I-CoN_4 sites, achieving a high NH_3 yield of 18.64 $mg \cdot h^{-1} \cdot mg_{cat}^{-1}$ and a maximum Faradaic efficiency of 97% under neutral conditions [22]. The similar tandem reaction was also found in the amorphous $CuCoO_x$ with enhanced active hydrogenation by Cu–Co synergy which accelerates the nitrate conversion [23]. A built-in electric field on the interface of Cu_xS and CoS_x was confined as a critical role for enhancing NO_3RR via accelerating the electron transferring and creating more active sites [24]. Such catalysts with multiple

Received: December 22, 2025; **Revised:** January 26, 2026
Accepted: January 30, 2026

✉Address correspondence to Muwei Ji, mwji@stu.edu.cn; Fushen Lu, fslu@stu.edu.cn

compositions was considered connecting the step reaction of NO_3^- → NO_2^- and NO_2^- → NH_3 with facile controlling [25]. Moreover, the rate-limiting step of NO_3^- → NO_2^- was generally breakout by using Cu sites.

In addition, among the reported catalysts, carbon-based catalysts are considered particularly prominent because of the extraordinary specific surface area and enhanced dispersity of catalystic sites [26–30]. It not only exhibits high electrical conductivity and high electron transfer efficiency [31, 32], but also may enhance the adsorption of reaction intermediates through heteroatom doping or surface defect sites [33]. Furthermore, it can anchor metal atoms on the carbon surface, thereby dispersing the catalytic centres to reduce the possible coupling of *N, which in turn results in higher NH_3 selectivity [34]. As reported by Zhang and his colleagues, Co was loaded onto N-doped carbon fiber cloth to construct an electron deficient Co nanocrystal, achieving a high NH_3-yield rate of 109 $mg \cdot h^{-1} \cdot cm^{-2}$ with a high Faradaic efficiency [35]. Beyond the catalyst modulation, the adsorption of NO_3^- at electrode is also critical for NO_3RR [36], as it can reduce the onset potentials and accelerate the kinetics. For example, CeO_2-C/$BiVO_4$ Lewis acid and base revealed an improved path for converting nitrate into ammonia [37]. Therefore, the constructed sites for enhancing the NO_3^- adsorption represent a potential strategy to promote the NO_3RR, although limited work has been reported on this aspect. In terms of catalyst design, boron (B) atoms or sites were Lewis acid centers and recognized as effective sites for adsorbing NO_3^- and thereby increasing its local concentration at electrode surface. Based on this strategy, B was doped into carbon nanotubes to synthesize B,N-doped carbon nanotubes (BNCNTs) loaded with copper iron bimetallic oxides (Cu_2O-Fe_3O_4) and then the obtained catalyst was employed to investigate NO_3RR, specifically dependent on the NO_3^- adsorbing.

2 Experimental

2.1 Chemical and regents

3,4,9,10-Perylenetetracarboxylic dianhydride (PTCDA) was purchased from Energy Chemical Reagent Co., Ltd. Dianhydride, urea, boric acid, NaClO solution (≥ 5 wt.%), potassium sodium tartrate, sodium nitroprusside, iron(III) chloride hexahydrate ($FeCl_3 \cdot 6H_2O$), and copper(II) chloride dihydrate ($CuCl_2 \cdot 2H_2O$) were purchased from Aladdin Reagent Co., Ltd. Ammonium chloride was purchased from Sigma-Aldrich Co., Ltd. The reagents were used without further purification.

2.2 Synthesis of B,N-doped carbon nanotubes

Boric acid (1.24 g), urea (14.4 g), and perylene tetracarboxylic dianhydride (1.76 g) were added to a mixed solvent consisting of 25 mL of 95% ethanol and 25 mL of water. Subsequently, the mixture was subjected to ultrasonic treatment for 10 min to achieve complete dispersion and dissolution of the components. Then, rotary evaporation was performed to remove most of the solvent, yielding a red viscous solid mixture. The mixture was dried in a vacuum oven at 70 °C for 8 h to ensure thorough drying. The mixture was transferred to an agate mortar and ground thoroughly. Once it turned into a uniform red powder, it was transferred to a corundum crucible. The pyrolysis treatment was proceeded in a tubular furnace: The mixture was heated to 800 °C at a rate of 10 °C·min^{-1} in an Ar atmosphere and the temperature was maintained for 3 h. Afterwards, it was allowed to cool naturally to room temperature in a Ar atmosphere. A spatula was used to transfer the obtained black solid to a mortar for further grinding. Subsequently, it was transferred to a beaker, an appropriate amount of water was added, and it was heated in an oil bath at 85 °C, stirring for 1 h to fully dissolve any unreacted urea. The mixture was filtered while it was still hot, and the filter cake was washed three to four times with hot water and ethanol. Finally, the filter cake was dried in a vacuum drying oven at 65 °C for 10 h to obtain the black product, B,N-doped carbon nanotubes.

2.3 Synthesis of Cu_2O-Fe_3O_4/BNCNTs

B,N-doped carbon nanotubes (100 mg), iron(III) chloride hexahydrate ($FeCl_3 \cdot 6H_2O$, 0.5 mmol), copper chloride dihydrate ($CuCl_2 \cdot 2H_2O$, 0.5 mmol), and sodium bicarbonate ($NaHCO_3$, 2 mmol) were added to 40 mL of 95% ethanol solution with stirring at room temperature for 10 h. The resulted mixture was filtered and washed (three times with ethanol). With Ar atmosphere protection, the product, Cu_2O-Fe_3O_4/BNCNTs, was obtained by treating at 400 °C for 3 h. The other metal oxides/BNCNTs samples were prepared with similar methods.

2.4 Electrochemical measurements

Typically, Cu_2O-Fe_3O_4/BNCNTs (5 mg) and Nafion solution (5 wt.%, 120 μL) were dispersed in alcohol (880 μL) and by ultrasonic treatment for 30 min. Then the resulted mixture was taken as ink (10 μL) and dropped onto a carbon paper (1 cm × 1 cm) at room temperature. The loaded Cu_2O-Fe_3O_4/BNCNTs on carbon paper is 0.05 $mg \cdot cm^{-2}$. The electrochemical measurements were tested by an electro-chemical workstation (CHI 660E, Chenhua, Shanghai). The "H-type" cell was adopted with a three-electrode system.

A carbon paper loaded with catalyst was used as the working electrode, the Ag/AgCl electrode was the reference electrode, and the platinum plate electrode was the opposite electrode. A mixed solution containing NaOH (0.1 $mol \cdot L^{-1}$) and $NaNO_3$ (0.1 $mol \cdot L^{-1}$) was taken as electrolyte. Because the produced NH_3 in alkaline environment evaporated out of the cell easily, H_2O (10 mL) was used to absorb the evaporated-NH_3 in a separated apparatus. The potentials were converted to a reversible hydrogen electrode (RHE) potential as follows

$$E_{RHE} = E_{Ag/AgCl} + 0.059\ pH + 0.197\ V \quad (1)$$

The cyclic voltammetry (CV) or linear sweep voltammetry (LSV) test ranged from −0.4 to −0.8 V_{RHE}.

2.5 Characterization

The X-ray diffraction (XRD) patterns were recorded on a Bruker D8 Advance Diffractometer. The scanning electron microscopy (SEM) images were taken on a Gemini 300 scanning electron microscope. The low-resolution transmission electron microscopy (TEM) and high-resolution TEM (HRTEM) images were obtained using a JEM-F200 microscope equipped with energy dispersive X-ray spectroscopy (EDS) detectors. The X-ray photoelectron spectroscopy (XPS) analysis was performed on an X-ray photoelectron spectrometer (Thermo Scientific K-Alpha) using monochromatic Al Kα radiation. The ultraviolet–visible (UV–Vis) absorption spectra were measured on a puxi UV-6 spectrophotometer (Beijing puxi General Instrument Co., Ltd.).

The low temperature nitrogen adsorption–desorption test was taken on an ASAP 2020M automatic surface and voids analyzer. The NO_3^- adsorption was obtained via a typical process: 10 mg of sample Cu_2O-Fe_3O_4/BNCNTs or Cu_2O-Fe_3O_4/NCNTs was added to 30 mL of 50 mg·L^{-1} sodium nitrate solution. After 10 min of reaction, the mixture was subjected to filtration, and the residual concentration of NO_3^- in the filtration was determined.

3 Results and discussion

As shown in Fig. 1(a), perylene tetracarboxylic dianhydride (PTCDA), urea, and boric acid were uniformly mixed in ethanol for trapping Cu^{2+} and Fe^{3+}, followed by the Cu_2O and Fe_3O_4 grew on the BNCNTs via pyrolysis process to form the Cu_2O-Fe_3O_4/BNCNTs. The XRD patterns of samples (Fig. 1(b)) exhibited a broad-strong peak at 26° and a weak peak at 44°, corresponding to the (002) and (004) planes of graphite carbon, respectively. No charactered diffraction peaks of copper oxides or iron oxides were observed, indicating the small size of Cu_2O and Fe_3O_4. For comparison, Cu_2O/BNCNTs and Fe_3O_4/BNCNTs were obtained by adding Cu^{2+} or Fe^{3+} with a similar strategy, and their XRD pattens also presented the diffraction peaks of graphite carbon without any peaks of metal oxides (Fig. S1 in the Electronic Supplementary Material (ESM)). Figure 1(c) displays the distinct tubular structure of BNCNTs with a smooth surface. Upon incorporating Cu^{2+} and Fe^{3+}, numerous particles appeared on the surface of BNCNTs with uniform dispersion (Fig. 1(d)), which were considered the Cu_2O and Fe_3O_4 nanoparticles. Notably, the sizes of such nanoparticles were so small that no discernible diffraction peak was observed in the XRD pattern [38–40]. Notwithstanding, the EDS element analysis presented that the Cu and Fe elements dispersed uniformly throughout the samples (Fig. 1(e)), verifying the successfully loading of Cu_2O and Fe_3O_4. The TEM image further confirms the little metal oxide nanoparticle attached onto the surface of carbon wall (Fig. 1(f)). The results of XPS semi-quantitative analysis demonstrate that the metal content is extremely low, which is also one of the reasons for the absence of distinct diffraction peaks in the XRD pattern (Table S1 in the ESM).

The HRTEM image shows the nanoparticles with clear lattice fringes loading on BNCNTs (Fig. 2(a)), while BNCNTs present an amorphous phase with a wall thickness of 10–20 nm (Figs. 2(b) and 2(c)). As displayed in Figs. 2(d) and 2(e), Cu^{2+} and Fe^{3+} never form the $CuFeO_x$ bimetallic oxides but the Cu_2O and Fe_3O_4 nanocrystals during the prepared process. The measured fringe space distances of 0.24 and 0.21 nm were assigned to the Fe_3O_4(311) (PDF #26-1136) and Cu_2O(200) (PDF #34-1354) planes, respectively (Figs. 2(d) and 2(e)). The fast Fourier transformed (FFT) images of Cu_2O-Fe_3O_4/BNCNTs show the presence of Fe_3O_4 and Cu_2O phases (Fig. S2 in the ESM), further confirming the successful preparation of Cu_2O-Fe_3O_4/BNCNTs. Meanwhile, the high-angle annular dark-field scanning transmission electron microscopy (HAADF-STEM) image (Fig. 2(f)) revealed numerous particles with bright contract on nanotubes. In addition, the Brunauer–Emmett–Teller (BET) area Cu_2O-Fe_3O_4/BNCNTs and Cu_2O-Fe_3O_4/NCNTs are 200 and 129 m^2·g^{-1} with average pore sizes of 22.2 and 21.4 nm, respectively (Fig. S3 in the ESM). This indicates that B doping does not cause a significant change in the physical structure of carbon nanotubes. The XPS survey spectrum of the Cu_2O-Fe_3O_4/BNCNTs (Fig. S4 in the ESM) displayed the sharp peaks for C, N, O, B, Fe, and Cu elements, further confirming the composite compositions. The high-

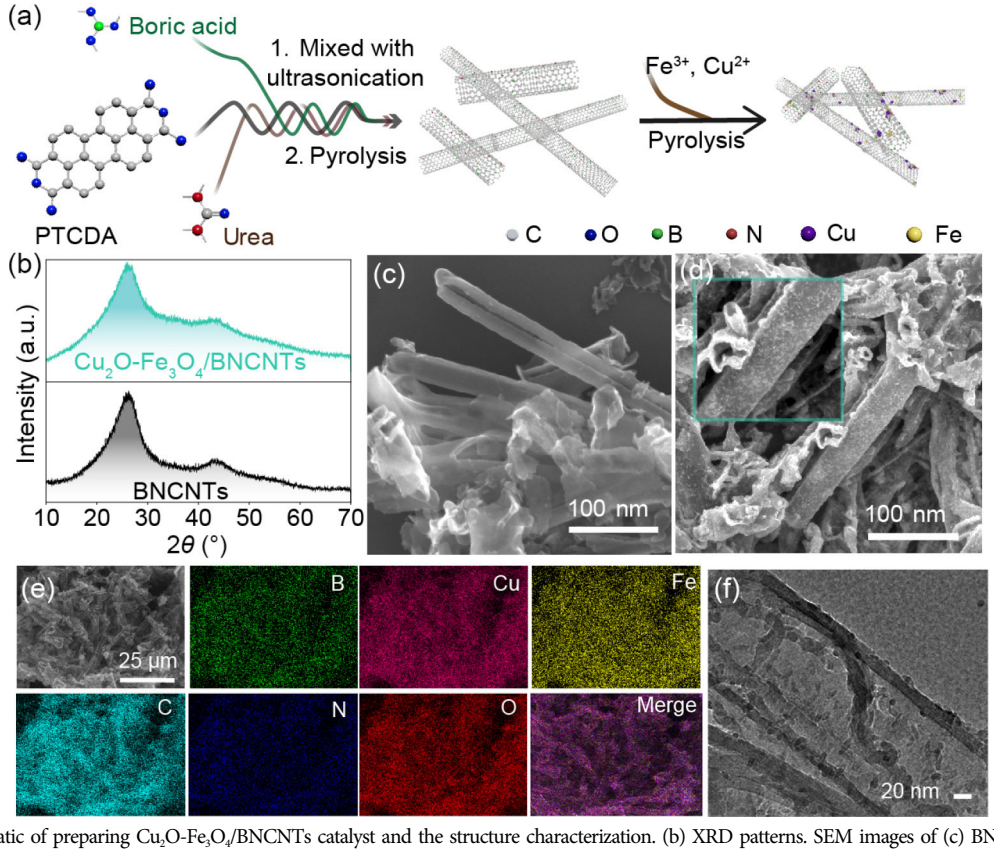

Figure 1 (a) Schematic of preparing Cu_2O-Fe_3O_4/BNCNTs catalyst and the structure characterization. (b) XRD patterns. SEM images of (c) BNCNTs and (d) Cu_2O-Fe_3O_4/BNCNTs. (e) SEM-EDS element mapping images and (f) TEM image of Cu_2O-Fe_3O_4/BNCNTs.

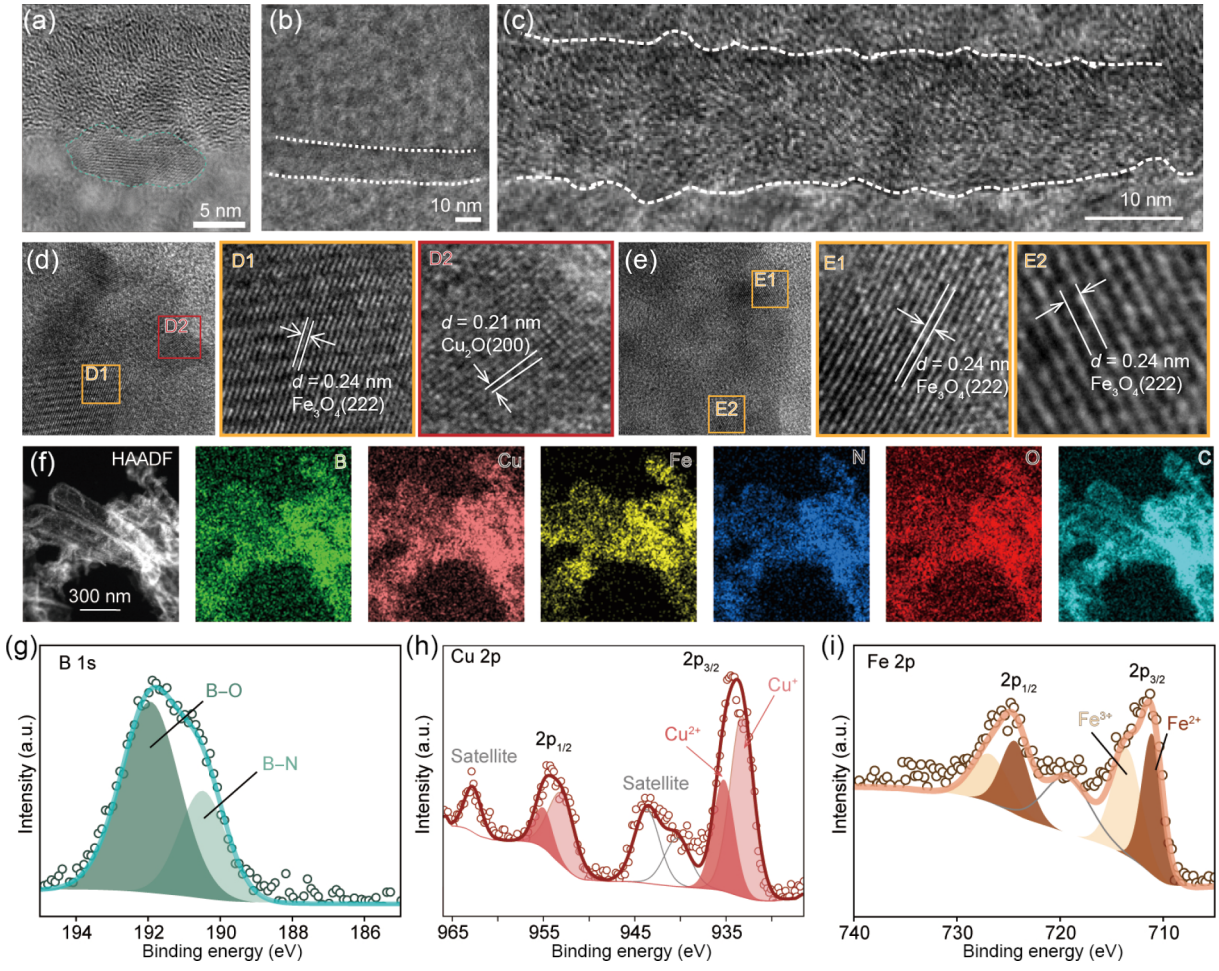

Figure 2 HRTEM images: (a) the Cu_2O-Fe_3O_4/BNCNTs, ((b) and (c)) the magnified images of carbon nanotube wall, and ((d) and (e)) the metal oxides on the BNCNTs. (f) HAADF-STEM image of Cu_2O-Fe_3O_4/BNCNTs and the corresponding element mapping. ((g)–(i)) The high-resolution XPS spectra of Cu_2O-Fe_3O_4/BNCNTs: (g) B 1s, (h) Cu 2p, and (i) Fe 2p.

resolution B 1s XPS spectrum (Fig. 2(g)) featured two peaks at 190.8 and 191.8 eV, corresponding to the B–N and B–O bonds, respectively [19], confirming B doping by the B–O and B–N binding within the carbon nanotube structures. The formation of B–O and B–N can be corroborated by comparing with the infrared spectra of undoped boron carbon nanotubes and boron nitride (BN) (Fig. S5 in the ESM). The high-resolution Cu 2p XPS spectrum (Fig. 2(h)) exhibited two peaks at 933 (Cu $2p_{1/2}$) and 953 eV (Cu $2p_{3/2}$), accompanied by the satellite peaks at 943.7 and 962.8 eV. After dealt with deconvolution, the peaks at 933.1 and 955.2 eV were assigned to the Cu^{2+}, while those at 933.3 and 953.2 eV correspond to the $2p_{3/2}$ and $2p_{1/2}$ of Cu^{2+}, respectively [23]. The high-resolution Fe 2p XPS spectrum (Fig. 2(i)) revealed two peaks at 710.3 and 729.5 eV, deconvoluted into Fe^{3+} and Fe^{2+}. Peaks at 710.3 (Fe^{2+} $2p_{3/2}$) and 723.8 eV (Fe^{2+} $2p_{1/2}$), along with peaks at 712.8 (Fe^{3+} $2p_{3/2}$) and 729.5 eV (Fe^{3+} $2p_{1/2}$), indicated the coexistence of $Fe^{2+}$and Fe^{3+} state. The peak at 717.2 eV was the satellite peak, which further confirmed the mixed stated of Fe, known to enhance NO_3RR [22]. Four deconvoluted peaks of C 1s (Fig. S6 in the ESM) were assigned to C–C bond (284.8 eV), C–O bond (286.4 eV), C–N bond (287.4 eV), and O=C–O bond (288.8 eV) [41]. The deconvoluted N 1s spectrum (Fig. S7 in the ESM) exhibited two peaks at 398.4 and 401.1 eV, belonging to pyridinic nitrogen and graphitic nitrogen, respectively [42]. In the deconvoluted O 1s XPS spectrum (Fig. S8 in the ESM), the peak at 530.2 eV is viewed as the B–O bond and the peaks at 531.9 and 533.3 eV are assigned to the bonds of C=O and C–O, respectively. Hence, the XPS characterization confirms the bonding of B dopant connected to the carbon nanotubes and further reveals the presence of metallic oxides for NO_3RR.

As presented in Fig. 3(a), the polarized plots of hydrogen evolution reaction (HER) on Cu_2O-Fe_3O_4/BNCNTs illustrated the onset potential at about −0.5 V_{RHE} in NaOH electrolyte while increasing the NO_3^- concentration to 0.1 mol·L^{-1}, and the onset potential positively shifted to 0.1 V_{RHE} with a higher current density across the whole tested potential window. The difference of performances in the two electrolyte solutions illustrates that NO_3RR on Cu_2O-Fe_3O_4/BNCNTs is driven more easily than HER. Besides, the NH_3 yield rate reaches 95.24 mg·h^{-1}·mg_{cat}^{-1} at −0.8 V_{RHE} but no any generated NH_3 is measured under open circuit potential or in the NaOH solution (Fig. 3(b)), demonstrating that the NH_3 yield after test is from NO_3RR rather than from the decomposition of BNCNTs. As shown in Fig. S9 in the ESM, the onset potential both on the Cu_2O-Fe_3O_4/BNCNTs and Cu_2O-Fe_3O_4/NCNTs positively shifted and the larger current density increased as the NO_3^- concentration escalates, with Cu_2O-Fe_3O_4/BNCNTs consistently exhibiting higher currents. In addition, a larger current density occurs at the present of NO_3^- and the current density at −0.8 V_{RHE}

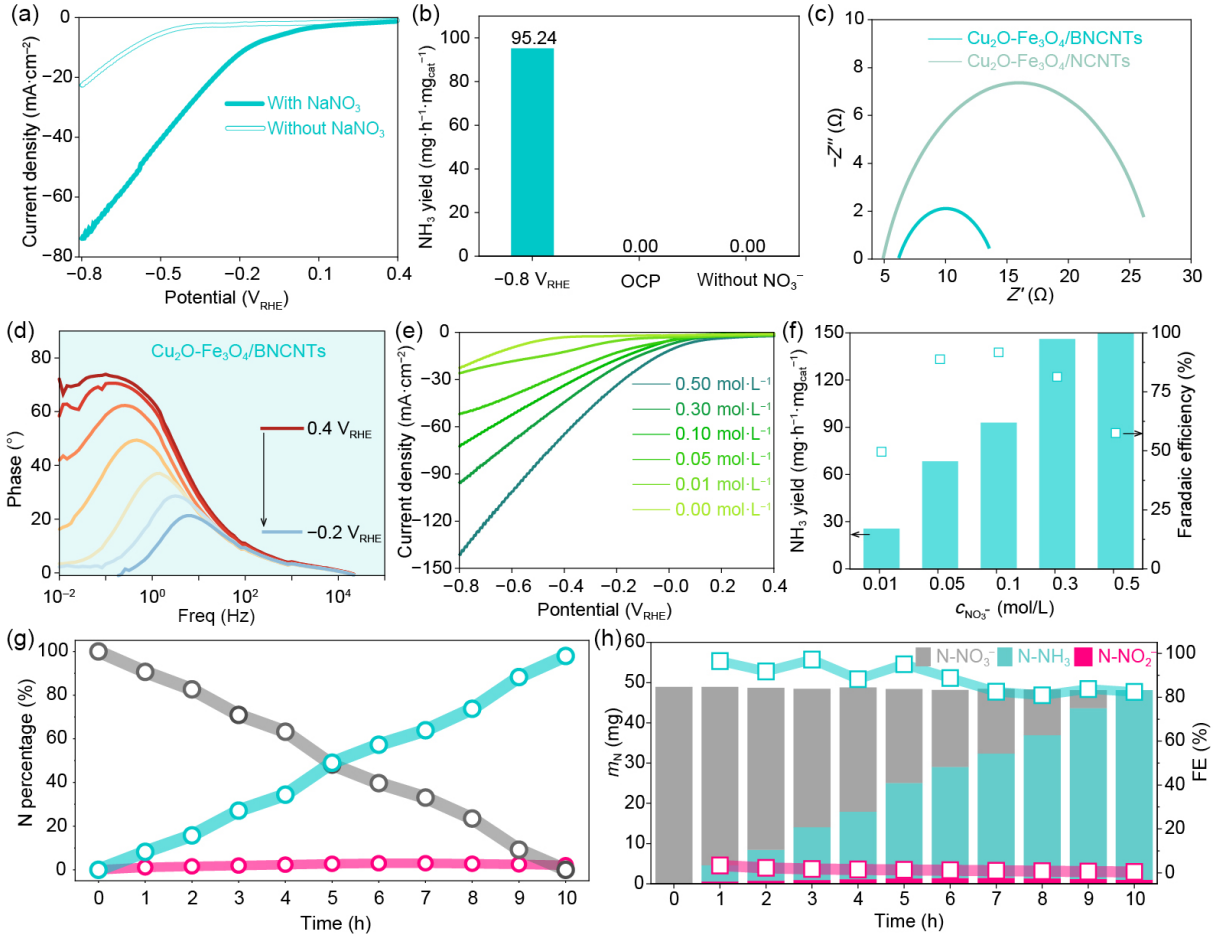

Figure 3 (a) LSV curves of the Cu_2O-Fe_3O_4/BNCNTs in the electrolyte of 0.1 mol·L^{-1} NaOH or 0.1 mol·L^{-1} NaOH-0.1 mol·L^{-1} $NaNO_3$. (b) NH_3 yield on the Cu_2O-Fe_3O_4/BNCNTs electrode. The EIS characterization: (c) Nyquist plots and (d) bode plots. (e) LSV curves on the Cu_2O-Fe_3O_4/BNCNTs in electrolyte with series of $NaNO_3$ concentration.(f) The NH_3 yield depending on $NaNO_3$ concentration, where the driven potential is −0.8 V_{RHE}. (g) The percentage of N species variation during NO_3RR and (h) the NO^{3-} and the produced NH_3 and NO^{2-} depending on time.

reaches 77 mA·cm^{-2}, which is three times larger than that observed on the BNCNTs, confirming the higher current density on Cu_2O-Fe_3O_4/BNCNTs from the enhanced activity to the Cu and Fe sites. As reported, on the CuFe-based bimetallic catalysts for NO_3RR, the active Cu sites are considered mainly transforming the NO_3^- into NO_2^-, while the Fe sites produce new active hydrogen for the formation of NH_3. The tandem reaction from Cu sites and Fe sites synergetically accelerate the yielded NH_3 rate [43, 44]. In our case, the Cu_2O and Fe_3O_4 nanoparticles grow on the BNCNTs independently due to no observed interface between the two phases. Hence, the catalysis on NO_3RR was driven with tandem reaction path. Moreover, although loaded Cu_2O and Fe_3O_4 nanoparticles at the same conditions, the Cu_2O-Fe_3O_4/NCNTs performed a lower current density and crucially, and B doping into the CNTs substrate also brings the more positive onset potential, indicating the the higher activity resulting from the enhanced adsorption of NO_3^- by B sites. Nyquist plots of the Cu_2O-Fe_3O_4/BNCNTs and the Cu_2O-Fe_3O_4/NCNTs present that B-dopant reduces the resistance of charge transferring (Fig. 3(c)). The Bode plots of Cu_2O-Fe_3O_4/BNCNTs at series of potentials illustrate that a high phase angle at the low frequency remains at a positive potential and drops down rapidly as the potential negative shifting (Fig. 3(d)), demonstrating the NO_3^- reduction in the series employed potentials. Compared to the Bode plots on Cu_2O-Fe_3O_4/NCNTs at the same potential range (Fig. S10 in the ESM), the phase angle on Cu_2O-Fe_3O_4/BNCNTs at 0.4 V_{RHE} is higher (reaching 80° at 0.1 Hz) while the phase angel on Cu_2O-Fe_3O_4/NCNTs remains about 60° in the potential range of 0.4 and 0.1 V_{RHE}. The phase angle difference is considered resulting from the more absorption of NO_3^- because the phase angle on Cu_2O-Fe_3O_4/BNCNTs reduces more rapidly, indicating the faster kinetics due to the high NO_3^- concentration. This conclusion is also supported by the BET measurement results of the materials. The nitrogen adsorption–desorption isotherm of Cu_2O-Fe_3O_4/BNCNTs exhibits an H3-type hysteresis loop [39, 45], and the hysteresis observed in the low-pressure desorption branch indicates a strong Lewis acid-base interaction between the material and nitrogen molecules. Although the specific surface area of Cu_2O-Fe_3O_4/BNCNTs (200 m^2·g^{-1}) is higher than that of Cu_2O-Fe_3O_4/NCNTs (129 m^2·g^{-1}) (Fig. S2 in the ESM), the results of static adsorption experiment present that the NO_3^- adsorption capacity of Cu_2O-Fe_3O_4/BNCNTs reaches 8107 μg·g^{-1}, 2.4 times that of Cu_2O-Fe_3O_4/NCNTs (3338 μg·g^{-1}) under the same conditions (Fig. S11 in the ESM). The LSV plots of Cu_2O-Fe_3O_4/BNCNTs (Fig. 3(e)) illustrate the positive shift of onset potential and promoted current density with increasing the NO_3^- concentration, confirming the performance of NO_3^- conversion depending on its concentration. The NH_3 yield rate also rises with increasing NO_3^- concentration

and reaches 148.8 $mg{\cdot}h^{-1}{\cdot}mg_{cat}^{-1}$ at the concentration of 0.5 $mol{\cdot}L^{-1}$ (Fig. 3(f)). Nevertheless, the corresponding Faradaic efficiency reaches the highest value (91.2%) with a NH_3 yield rate of 93.1 $mg{\cdot}h^{-1}{\cdot}mg_{cat}^{-1}$ at 0.1 $mol{\cdot}L^{-1}$ concentration, while reduces to 62.1% when the concentration continues enlarging to 0.5 $mol{\cdot}L^{-1}$. The inconsistence in change trend depending on NO_3^- concentration is viewed from the different rates of NO_3^- conversion and proton providence. Although the large NO_3^- concentration promotes the kinetics of the NO_3^- conversion, the rate of proton reduction never rises with increasing the NO_3^- concentration and thus the hydrogenation of nitrate is limited. As shown in Fig. S12 in the ESM, the yielded speed of NO_2^- at the high NO_3^- concentration reaches at about 60 $mg{\cdot}h^{-1}{\cdot}mg_{cat}^{-1}$, near 50% of yielded NH_3. The massive accumulation of NO_2^- occupies the active sites, thereby inhibiting the generation of *H. Noteworthy, the B dopant does not enhance the proton adsorption so that the further enhancement on Cu_2O-Fe_3O_4/BNCNTs is not observed at more negative potentials, illustrating that B sites mainly play a Lewis acid to concentrate the NO_3^- on the surface of electrode. The similar concentration-dependent behavior of both catalysts confirms that the Cu and Fe sites provide the main catalytic activity for NO_3RR, while the performance difference between Cu_2O-Fe_3O_4 /BNCNTs and Cu_2O-Fe_3O_4/NCNTs (Fig. 3(e) and Fig. S13 in the ESM) stems from the presence of B dopant sites. Under −0.8 V_{RHE} of driven potential, N species in the electrocatalytic system were measured to reveal the performance details of Cu_2O-Fe_3O_4/BNCNTs. As shown in Fig. 3(g), the nitrate concentration reduces linearly depending on the reaction time, while the NH_3 yield increases correspondingly. The percentage of NO_2^- remains a low level across the whole test period, illustrating the well matching of tandem reaction of NO_3^- reduction and hydrogenation. Figure 3(h) presents the total mass of N species remains about 49 mg during 10 h of electrocatalysis with stable Faradaic efficiency of NO_3^- (~ 90%) and NO_2^- (~ 5%), illustrating transformations of NO_3^- into NO_2^- and NH_3 without other side products.

By controlling the added amount of B source, series of Cu_2O-Fe_3O_4/BNCNTs were obtained (Tables S2 and S3 in the ESM). The SEM images (Figs. S14–S17 in the ESM) show that the different amount of added B source never changes the morphologies, demonstrating our strategy for preparing metal oxides/BNCNTs with well tailoring. Notwithstanding, when the feed boric acid increase to 10%, the morphology of obtained samples is not nanotube (Fig. S18 in the ESM), and thus such samples are not investigated so that the NO_3RR performance can be compared at the same conditions. The electrocatalytic activities of series of Cu_2O-Fe_3O_4/BNCNTs on NO_3RR were closed with similar onset potential and current density at same driven potentials, illustrating the activities mainly from Cu_2O and Fe_3O_4 (Fig. 4(a)). Notwithstanding, the higher activity of Cu_2O-Fe_3O_4/BNCNTs than that of Cu_2O-Fe_3O_4/NCNTs reveals the enhancement from B dopant into the CNTs. The Nyquist plots (Fig. 4(b)) on series of Cu_2O-Fe_3O_4/BNCNTs samples present that the introduction of B does not

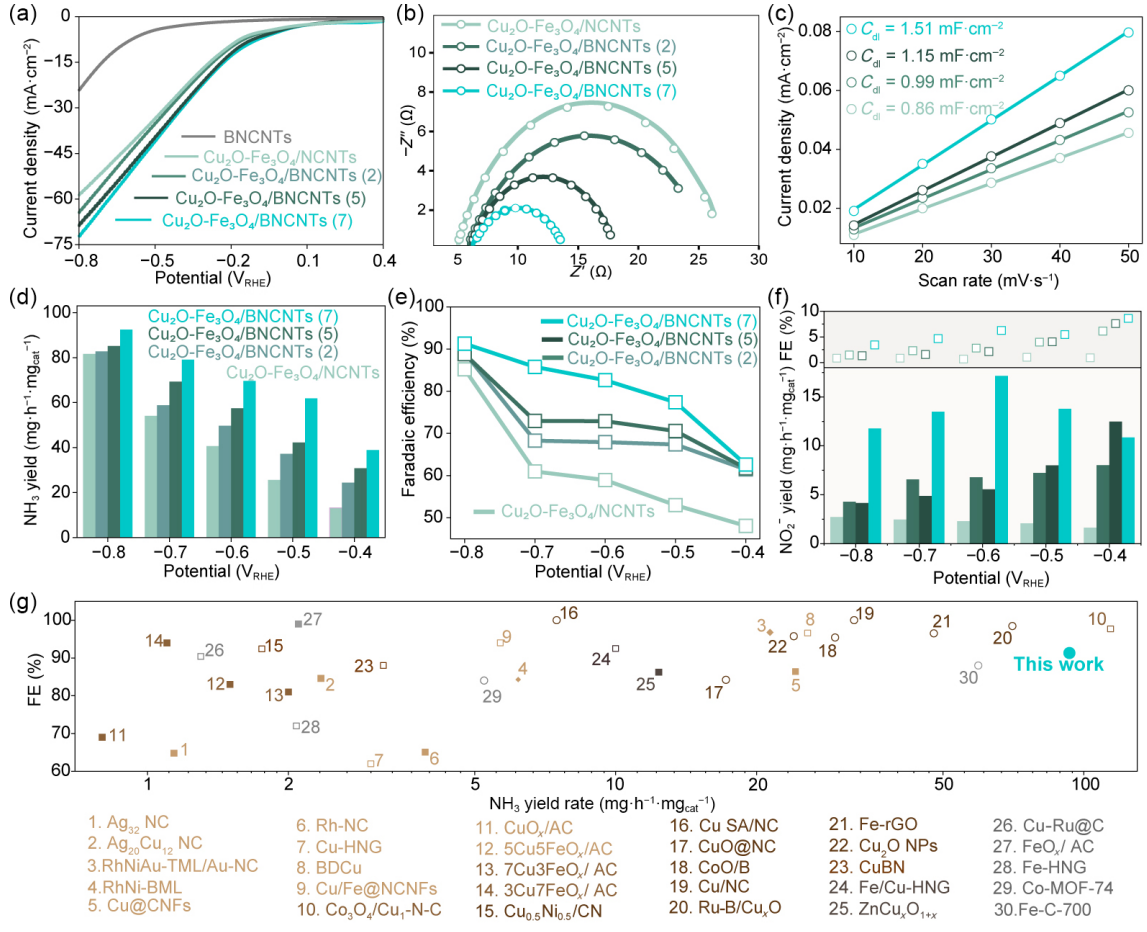

Figure 4 (a) Comparison of LSV curves of series of the Cu_2O-Fe_3O_4/BNCNTs and the BNCNTs. (b) EIS plots. (c) C_{dl} measured in the NaOH-$NaNO_3$ mixed solution. NO^{3-} reduction performance on series of Cu_2O-Fe_3O_4/BNCNTs: (d) NH_3 yield on Cu_2O-Fe_3O_4/BNCNTs at various potentials and (e) the Faradaic efficiency. (F) NO^{2-} yield and the corresponding FE. (g) The NH_3-production comparison of the and the Cu_2O-Fe_3O_4/BNCNTs.

influence on the contact resistance but the charge transferred resistance (R_{ct}). By fitting the electrochemical impedance spectroscopy (EIS) with simulated circles (Fig. S19 in the ESM), the R_{ct} of Cu_2O-Fe_3O_4/BNCNTs (7) sample is calculated to be the lowest value of 5.9 Ω, illustrating the fastest kinetics. Noting the Fe and Cu as main electrocatalytic sites, B sites are considered to increase the NO_3^- concentration on the surface of electrode, thereby accelerating the NO_3^- conversion with inhibiting H_2 production. As shown in Fig. 4(c) and Figs. S20–S23 in the ESM, the C_{dl} results measured in NaOH-$NaNO_3$ mixed solution present the value slightly rise as the increasement of added B, which resulted from the NO_3^- absorption. Based on the enhanced absorption of NO_3^-, the yielded NH_3 products obtained in different driven potential were measured and the dependence of NH_3 products on the B doping was further testified (Fig. 4(d)). Notably, the corresponding Faradaic efficiencies display similar trends but the Cu_2O-Fe_3O_4/BNCNTs electrodeperformed higher efficiencies than Cu_2O-Fe_3O_4/NCNTs electrode (Fig. 4(e)), illustrating the hydrogen evolution inhabitation from the high NO_3^- concentration in some degree. Although the generated NO_2^- concentration and Faradaic efficiencies remain at low levels, the amount of NO_2^- generated on Cu_2O-Fe_3O_4/BNCNTs is higher than that on Cu_2O-Fe_3O_4/NCNTs (Fig. 4(f)), revealing faster conversion of NO_3^- and large consumption of hydrogen reducing the HER. Consequently, the doped B sites in the CNTs play as Lewis acid sites for enhancing NO_3^- absorption and thus accelerate the NO_3RR with inhabitation of HER. Compared to the reported catalysts [30, 46–65], the Cu_2O-Fe_3O_4/BNCNTs in our work showed a competitive activity with high NH_3 yield rate and Faradaic efficiency (Fig. 4(g)), highlighting the potential of BNCNTs as substrate for enhancing the electrocatalysis on NO_3RR via the dopant B sites. Furthermore, during the 10-cycle test, this material not only maintained a Faradaic efficiency of over 90% and a high ammonia yield (Fig. S24 in the ESM) but also exhibited a stable current density (Fig. S25 in the ESM), a result that verifies its excellent catalytic stability.

Furthermore, the BNCNTs were taken as substrate to form metal oxides/BNCNTs (Figs. S26–S30 in the ESM) for NO_3RR and the electrocatalytic activities are present in Fig. 5. As displayed in Fig. 5(a), the Cu_2O/BNCNTs also performed with slightly higher activity than Cu_2O/NCNTs because Cu sites are viewed as active sites for adsorbing and conversing NO_3^- into NO_2^- and thus the B sites play weak roles on the NO_3^- reduction at the absence of catalytic site for hydrogenation. On the BNCNT substrate, the growth of metal oxides (Fe_3O_4, Co_3O_4, and NiO) for hydrogenation (Figs. 5(b)–5(d)) highlight the NO_3RR enhancement by B sites concentrating NO_3^- on the surface of electrodes. Additionally, Mn_2O_3/BNCNTs perform a poorer activity on NO_3RR but higher than Mn_2O_3/NCNTs, further confirming the activity of metal oxide/BNCNTs from metal sites while B sites promoting the NO_3^- adsorption. Consequently, B doping on the NCNTs combining with active sites is a general way for accelerating NO_3RR via enriching the NO_3^- on the electrode surface. As shown in Fig. 5(f) and Fig. S31 in the ESM, the ammonia yield represented by the bar chart is consistently higher for B-doped materials than for their undoped counterparts, and the same trend is observed for the Faradaic efficiency denoted by the square data points. The work provides a new horizontal for enhancing NO_3RR via concentrating the NO_3^- on the surface of electrodes which also lower the employed voltage and save the energy consumption.

4 Conclusions

In summary, B-doped sites of BNCNTs were constructed by adding H_3BO_3 to the mixture of carbonization precursor then combined with Cu_2O and Fe_3O_4 to form Cu_2O-Fe_3O_4/BNCNTs. Based on the tandem reaction of NO_3RR on Cu sites and Fe sites, Cu_2O-Fe_3O_4/BNCNTs perform a high activity with over 90% of average Faradaic efficiency. By comparing to the BNCNTs and Cu_2O-Fe_3O_4/NCNTs, B sites are confirmed concentrating NO_3^- on the surface of electrocatalyst and consequently positive shift the onset potential. The role of B dopants is also testified in series of metal

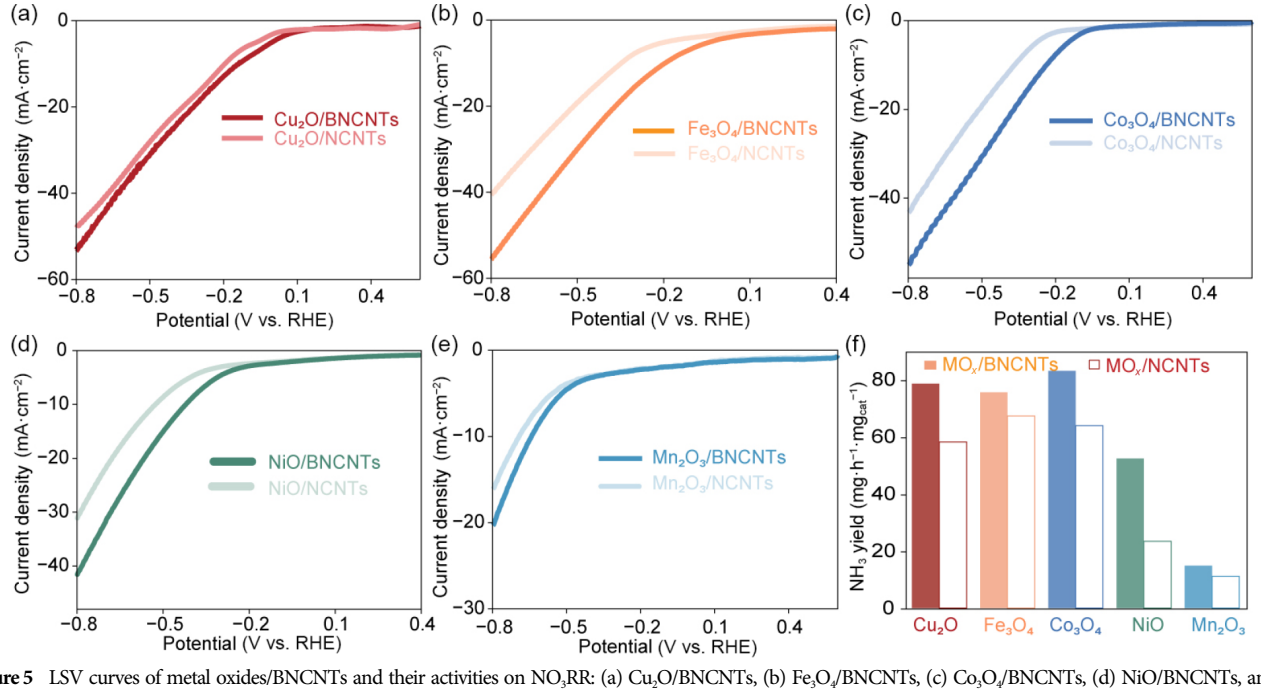

Figure 5 LSV curves of metal oxides/BNCNTs and their activities on NO_3RR: (a) Cu_2O/BNCNTs, (b) Fe_3O_4/BNCNTs, (c) Co_3O_4/BNCNTs, (d) NiO/BNCNTs, and (e) Mn_2O_3 /BNCNTs. (f) The corresponding NH_3 yield.

oxides/BNCNTs, illustrating the general strategy for designing and constructing efficient NO_3RR catalysts with enhanced NO_3RR and low energy consumption.

Electronic Supplementary Material: Supplementary material (the additional XRD patterns, XPS, IR spectrum, SEM, TEM images, and the corresponding electrocatalytic curves) is available in the online version of this article at https://doi.org/10.26599/NR.2026.94908512.

Data availability

All data needed to support the conclusions in the paper are presented in the manuscript and the Electronic Supplementary Material. Additional data related to this paper may be requested from the corresponding author upon request.

Acknowledgements

This work was supported by Shantou Scientific Research Initiation (No. NTF22018), Guangdong Basic and Applied Basic ResearchFoundation (Nos. 2025A1515010343, 2023A1515010562, and 2026A1515010751), Special Fund for the Sci-tech Innovation Strategy of Guangdong Province (No. STKJ202209083), and the Innovation Team Project of Guangdong Provincial Department ofEducation (No. 2023KCXTD012).

Declaration of competing interest

All the contributing authors report no conflict of interests in this work.

Author contribution statement

C. Z.: Data curation, validation, writing manuscript, experimental design. Y. T. H. and C. Q. L.: Data curation, project administration, validation, experimental design. C. X. W. and W. J. F.: Validation, experimental design. H. X.: Project administration. Y. B. S.: Project administration, writing manuscript. M. W. J.: Project administration, writing manuscript, funding acquisition. F. S. L.: Project administration, funding acquisition, writing manuscript. All the authors have approved the final manuscript.

Use of AI statement

None.

References

[1] Mingolla, S.; Rosa, L. Low-carbon ammonia production is essential for resilient and sustainable agriculture. *Nat. Food* **2025**, *6*, 610–621.

[2] Jiang, H. X.; Li, T. Y.; Gao, Y. T.; Fan, J. P.; Gan, D. W.; Yuan, S.; Hong, L. F.; Feng, Y.; Sun, J.; Song, Q. et al. Sustainable ammonia synthesis: Opportunities for electrocatalytic nitrate reduction. *J. Energy Chem.* **2025**, *105*, 630–668.

[3] Duan, G. Y.; Chen, Y. M.; Tang, Y.; Gasem, K. A. M.; Wan, P. Y.; Ding, D.; Fan, M. H. Advances in electrocatalytic ammonia synthesis under mild conditions. *Prog. Energy Combust. Sci.* **2020**, *81*, 100860.

[4] Theerthagiri, J.; Park, J.; Das, H. T.; Rahamathulla, N.; Cardoso, E. S. F.; Murthy, A. P.; Maia, G.; Vo, D. V. N.; Choi, M. Y. Electrocatalytic conversion of nitrate waste into ammonia: A review. *Environ. Chem. Lett.* **2022**, *20*, 2929–2949.

[5] Xu, H.; Ma, Y. Y.; Chen, J.; Zhang, W. X.; Yang, J. P. Electrocatalytic reduction of nitrate-a step towards a sustainable nitrogen cycle. *Chem. Soc. Rev.* **2022**, *51*, 2710–2758.

[6] Zhang, Z. Q.; Zhang, N.; Zhang, J.; Deng, B. Q.; Cao, Z. Y.; Wang, Z. B.; Wei, G. F.; Zhang, Q. B.; Jia, R. Y.; Xiang, P. Y. et al. Critical review in electrocatalytic nitrate reduction to ammonia towards a sustainable nitrogen utilization. *Chem. Eng. J.* **2024**, *483*, 148952.

[7] Kim, K.; Zagalskaya, A.; Ng, J. L.; Hong, J.; Alexandrov, V.; Pham, T. A.; Su, X. Coupling nitrate capture with ammonia production through bifunctional redox-electrodes. *Nat. Commun.* **2023**, *14*, 823.

[8] Hamsa, A. P.; Arulprakasam, M.; Unni, S. M. Electrochemical nitrogen fixation on single metal atom catalysts. *Chem. Commun.* **2023**, *59*, 10689–10710.

[9] An, R. S.; Wang, C. L.; Li, Y. D.; Di, Y. K.; Li, F. S.; Li, F.; Sun, L. C.; Wu, X. J. Amorphous/crystalline heterostructure nickel-cobalt oxides with rich oxygen vacancies for electrocatalytic production of benzoic acid coupled with nitrate reduction. *ACS Nano* **2025**, *19*, 17490–17502.

[10] Bai, W. T.; Zeng, H. Y.; Chen, F. J.; Wu, S. S.; Wang, S. C.; Du, Y. P.; Liu, S. L.; Wang, D. S.; Dai, Z. H. Emerging atomistic modeling catalysts for C-N electrocatalysis. *Adv. Mater.* **2026**, *38*, e10907.

[11] Liu, H. M.; Bai, L. C.; Bergmann, A.; Cuenya, B. R.; Luo, J. S. Electrocatalytic reduction of nitrogen oxide species to ammonia. *Chem* **2024**, *10*, 2963–2986.

[12] Zhang, H. R.; Wang, H. J.; Cao, X. Q.; Chen, M. S.; Liu, Y. L.; Zhou, Y. T.; Huang, M.; Xia, L.; Wang, Y.; Li, T. S. et al. Unveiling cutting-edge developments in electrocatalytic nitrate-to-ammonia conversion. *Adv. Mater.* **2024**, *36*, 2312746.

[13] Liu, K.; Li, H. M.; Xie, M. H.; Wang, P. F.; Jin, Z. Y.; Liu, Y. T.; Zhou, M.; Li, P. P.; Yu, G. H. Thermally enhanced relay electrocatalysis of nitrate-to-ammonia reduction over single-atom-alloy oxides. *J. Am. Chem. Soc.* **2024**, *146*, 7779–7790.

[14] Zhou, H. Y.; Wang, Q.; Pan, Y.; Pan, S.; Cui, D.; Bai, J. R. Research progress on alloy catalysts in the electrocatalytic reduction of nitrates for ammonia production. *J. Power Sources* **2026**, *678*, 240070.

[15] Yang, S.; Wei, H. X.; Xia, H.; Hu, L. S.; Song, Y. B.; Ji, M. W.; Lu, F. S. Bimetallic interface of RuCu hollow nanostructures combined with B_4C for enhancing electrocatalysis on nitrate reduction. *ACS Sustain. Chem. Eng.* **2024**, *12*, 3355–3363.

[16] Cai, J. M.; Wei, Y. Y.; Cao, A.; Huang, J. J.; Jiang, Z.; Lu, S. Y.; Zang, S. Q. Electrocatalytic nitrate-to-ammonia conversion with ~ 100% Faradaic efficiency via single-atom alloying. *Appl. Catal. B: Environ.* **2022**, *316*, 121683.

[17] Kim, H.; Lim, T. J.; Eom, H. H.; Kim, Y. J.; Kim, K.; Lee, J. W. Reconstructed fluorine doped perovskites for electrocatalytic urea production through reaction pathways with CO_2 and nitrate ions. *Appl. Catal. B: Environ. Energy* **2025**, *365*, 124974.

[18] Lu, H.; Opoku, K. N.; Wang, Z. X.; Ni, R. T.; Liu, M. T.; Wang, Y. Y.; Zhang, Y. P.; Yu, C.; Yuan, A. H.; Yang, F. et al. Electron-deficient asymmetric Co centers marry oxygen vacancy for NO_3RR: Excellent activity and anion resistance property. *Chem. Eng. J.* **2025**, *503*, 158536.

[19] Li, J.; Zhan, G. M.; Yang, J. H.; Quan, F. J.; Mao, C. L.; Liu, Y.; Wang, B.; Lei, F. C.; Li, L. J.; Chan, A. W. M. et al. Efficient ammonia electrosynthesis from nitrate on strained ruthenium nanoclusters. *J. Am. Chem. Soc.* **2020**, *142*, 7036–7046.

[20] Zhu, S. S.; Liu, K. Y.; Feng, Z.; Jiang, H. M.; Lin, J. J. The dual active site Ni_3Sn_2-$NiSnO_x$ alloy-oxide catalysts via Sn-modulated Ni coordination for efficient ammonia synthesis. *Nano Res. Energy* **2025**, *4*, e9120188.

[21] Lv, S. Y.; Yang, H. Y.; Hong, Q. L.; Xiao, X.; Chen, Y. Valence state engineering of copper oxide nanorods: A unified catalyst platform for efficient cathodic nitrate reduction and anodic glycerol oxidation. *Nano Res.* **2025**, *18*, 94907878.

[22] Cui, Z. J.; Wang, H. H.; Li, C. L.; Peng, W. C.; Liu, J. P. Iodine

dopants facilitate tandem catalysis via transformation adsorption behavior for efficient electrochemical nitrate reduction reaction. *ACS Nano* **2025**, *19*, 31050–31064.

[23] Deng, A. M.; Liu, J. J.; Li, Q. Y.; Wu, Z.; Wei, J. L.; Liu, J. N.; Chen, T.; Liu, H. W.; Zhang, Y. Q.; Wang, S. Y. Amorphous $CuCoO_x$ boosts active hydrogen for high-rate tandem electroreduction of nitrate to ammonia. *Small*, in press, https://doi.org/10.1002/smll.202501980.

[24] Zhang, M. L.; Zhang, Z. D.; Zhang, S. L.; Zhuang, Z. C.; Song, K. P.; Paramaiah, K.; Yi, M. Y.; Huang, H.; Wang, D. S. Efficient electrochemical nitrate reduction to ammonia driven by a few nanometer-confined built-in electric field. *ACS Catal.* **2024**, *14*, 10437–10446.

[25] Li, J.; Wang, Y.; Xing, X. J.; Wang, Y.; Xiong, W.; Li, H. Advancing electrochemical nitrate reduction: Overcoming rate-limiting bottlenecks with copper/cobalt catalysts. *Adv. Funct. Mater.* **2025**, *35*, e13717.

[26] Wan, Y. C.; Zhou, H. J.; Zheng, M. Y.; Huang, Z. H.; Kang, F. Y.; Li, J.; Lv, R. T. Oxidation state modulation of bismuth for efficient electrocatalytic nitrogen reduction to ammonia. *Adv. Funct. Mater.* **2021**, *31*, 2100300.

[27] Khan, F. S. A.; Mubarak, N. M.; Tan, Y. H.; Khalid, M.; Karri, R. R.; Walvekar, R.; Abdullah, E. C.; Nizamuddin, S.; Mazari, S. A. A comprehensive review on magnetic carbon nanotubes and carbon nanotube-based buckypaper for removal of heavy metals and dyes. *J. Hazard. Mater.* **2021**, *413*, 125375.

[28] Lu, Z. Q.; Wang, X.; Zong, H. W.; Lan, D.; Sun, Y. S.; Zhao, K.; Wang, B. B.; Liu, J. Q. Construction of flexible and self-supported $NiCo_2$Mn-LDH@Fe_2O_3 electrode materials with hierarchical core/shell heterostructures on carbon cloths for high-performance asymmetrical supercapacitors. *Chem. Eng. J.* **2024**, *500*, 157183.

[29] Liu, Y.; Shen, Y. T.; Sun, L. T.; Li, J. C.; Liu, C.; Ren, W. C.; Li, F.; Gao, L. B.; Chen, J.; Liu, F. C. et al. Elemental superdoping of graphene and carbon nanotubes. *Nat. Commun.* **2016**, *7*, 10921.

[30] Wang, T.; Niu, L. Y.; Zhang, K. J.; Wang, Y. S.; Guo, H. R.; He, X. S.; Xian, H. H.; Li, T. S. Carbon nanofiber-supported Cu nanoparticles for efficient nitrate reduction to ammonia. *Chem. Commun.* **2025**, *61*, 3532–3535.

[31] Chen, Q. R.; Liang, J.; Yue, L. C.; Luo, Y. S.; Liu, Q.; Li, N.; Alshehri, A. A.; Li, T. S.; Guo, H. R.; Sun, X. P. CoO nanoparticle decorated N-doped carbon nanotubes: A high-efficiency catalyst for nitrate reduction to ammonia. *Chem. Commun.* **2022**, *58*, 5901–5904.

[32] Zhao, X.; Jia, X. X.; He, Y. N.; Zhang, H. B.; Zhou, X. H.; Zhang, H. C.; Zhang, S. S.; Dong, Y. M.; Hu, X.; Kuklin, A. V. et al. Two-dimensional BCN matrix inlaid with single-atom-Cu driven electrochemical nitrate reduction reaction to achieve sustainable industrial-grade production of ammonia. *Appl. Mater. Today* **2021**, *25*, 101206.

[33] Xue, Y. H.; Yu, Q. H.; Ma, Q.; Chen, Y. Y.; Zhang, C. N.; Teng, W.; Fan, J. W.; Zhang, W. X. Electrocatalytic hydrogenation boosts reduction of nitrate to ammonia over single-atom Cu with Cu(I)-N_3C_1 sites. *Environ. Sci. Technol.* **2022**, *56*, 14797–14807.

[34] Zhao, X.; Jia, X. X.; Zhang, H. B.; Zhou, X. H.; Chen, X.; Wang, H. S.; Hu, X.; Xu, J.; Zhou, Y. T.; Zhang, H. C. et al. Atom-dispersed copper and Nano-palladium in the boron-carbon-nitrogen matric cooperate to realize the efficient purification of nitrate wastewater and the electrochemical synthesis of ammonia. *J. Hazard. Mater.* **2022**, *434*, 128909.

[35] Yang, B. P.; Zhou, Y. L.; Huang, Z. C.; Mei, B. B.; Kang, Q.; Chen, G.; Liu, X. H.; Jiang, Z.; Liu, M.; Zhang, N. Electron-deficient cobalt nanocrystals for promoted nitrate electrocatalytic reduction to synthesize ammonia. *Nano Energy* **2023**, *117*, 108901.

[36] Liu, M. J.; Fernández Otero, C. A.; Patino, D. U.; Gong, H. X.; Hossain, M. D.; Matthews, J. E.; Williams, K. S.; Vargas, A.; Zachman, M. J.; Hoffman, A. S. et al. Titanium-, nitrogen-doped carbon flowers catalyze electrochemical nitrate reduction reaction to ammonia. *J. Am. Chem. Soc.* **2025**, *147*, 29026–29041.

[37] Bai, H. Y.; Wang, F. F.; Ding, Q. J.; Xie, W. R.; Li, H. P.; Zheng, G. L.; Fan, W. Q. Construction of frustrated lewis pair sites in CeO_2-C/$BiVO_4$ for photoelectrochemical nitrate reduction. *Inorg. Chem.* **2023**, *62*, 2394–2403.

[38] Li, J. S.; Wang, Y.; Liu, C. H.; Li, S. L.; Wang, Y. G.; Dong, L. Z.; Dai, Z. H.; Li, Y. F.; Lan, Y. Q. Coupled molybdenum carbide and reduced graphene oxide electrocatalysts for efficient hydrogen evolution. *Nat. Commun.* **2016**, *7*, 11204.

[39] Hu, C.; Wang, Y.; Peng, K. S.; Wang, X. B.; Shen, Y. J.; Yang, K. W.; Hu, F.; Hung, S. F.; Wu, Y. P.; Ramakrishna, S. et al. Lewis acid adsorption promotes CO_2 enrichment for efficient formic acid electrosynthesis on reconstructed $Bi_2O_2CO_3$ in acidic media. *Angew. Chem., Int. Ed.* **2026**, *65*, e202512476.

[40] Peng, H. Y.; Wang, W. Y.; Gao, J. Y.; Jiang, F.; Li, B. W.; Wang, Y. C.; Wu, Y. Q.; Wang, Y.; Li, J. Q.; Peng, J. et al. Symmetry breaking in rationally designed copper oxide electrocatalyst boosts the oxygen reduction reaction. *Adv. Sci.* **2025**, *12*, 2411928.

[41] Wang, K.; Zhang, G. K.; Li, J.; Li, Y.; Wu, X. Y. 0D/2D Z-scheme heterojunctions of bismuth tantalate quantum dots/ultrathin g-C_3N_4 nanosheets for highly efficient visible light photocatalytic degradation of antibiotics. *ACS Appl. Mater. Interfaces* **2017**, *9*, 43704–43715.

[42] Xu, C. C.; Su, Y.; Liu, D. J.; He, X. Q. Three-dimensional N,B-doped graphene aerogel as a synergistically enhanced metal-free catalyst for the oxygen reduction reaction. *Phys. Chem. Chem. Phys.* **2015**, *17*, 25440–25448.

[43] Liu, Y. X.; Zhang, X.; Feizpoor, S.; Chen, H. C.; Li, L. F.; Zuo, Y. P.; Tian, S. J.; Liu, M. N.; Hu, W. Y.; Humayun, M. et al. Embedded Fe–Cu pairs enable tandem nitrate-to-ammonia electroreduction. *Adv. Mater.* **2026**, *38*, e14840.

[44] Cheng, X. T.; Zhao, H. L.; Liu, P. F.; Han, R. H.; Wang, Y. Q. A Cu/Fe_3O_4@CN tandem catalyst for efficient ammonia electrosynthesis from nitrate reduction. *J. Colloid Interface Sci.* **2025**, *682*, 703–714.

[45] Mishra, V.; Ramasamy, S.; Singh, D. L.; Merlin, P.; Gangavarapu, R. R. Role of Lewis acidity and optimum contribution of cobalt and iron on the adsorption and electrochemical reduction of N_2 to NH_3. *Catal. Today* **2025**, *445*, 115054.

[46] Yang, H. Y.; He, K. Y.; Ai, X.; Liu, X.; Yang, Y.; Yin, S. B.; Jin, P. J.; Chen, Y. Pyridine functionalized silver nanosheets for nitrate electroreduction. *J. Mater. Chem. A* **2023**, *11*, 16068–16073.

[47] Yin, H. B.; Dong, F.; Su, H. W.; Zhuang, Z. C.; Wang, Y. L.; Wang, D. S.; Peng, Y.; Li, J. H. Unraveling the activity trends and design principles of single-atom catalysts for nitrate electrocatalytic reduction. *ACS Nano* **2023**, *17*, 25614–25624.

[48] Yin, H. B.; Dong, F.; Wang, Y. L.; Su, H. W.; Li, X. S.; Peng, Y.; Duan, H. H.; Li, J. H. Understanding the activity trends in electrocatalytic nitrate reduction to ammonia on Cu catalysts. *Nano Lett.* **2023**, *23*, 11899–11906.

[49] Zhang, S.; Wu, J. H.; Zheng, M. T.; Jin, X.; Shen, Z. H.; Li, Z. H.; Wang, Y. J.; Wang, Q.; Wang, X. B.; Wei, H. et al. Fe/Cu diatomic catalysts for electrochemical nitrate reduction to ammonia. *Nat. Commun.* **2023**, *14*, 3634.

[50] Dai, L. J.; Li, S. J.; Dai, Y.; Zheng, Y. J.; Liu, K. H.; Li, H. X.; Jiang, B. Engineering CoO/B heterojunction electrocatalysts for boosting electrocatalytic nitrate reduction to ammonia. *Chem. Eng. J.* **2024**, *498*, 155735.

[51] Li, J.; Wang, B. L.; Wang, H. J.; Jia, J. Z.; Zhang, J. H.; Zhang, L. Y.; Tu, M. D.; Li, H.; Xu, C. L. Ru-doped ultrasmall Cu nanoparticles decorated with carbon for electroreduction of nitrate to ammonia. *Inorg. Chem.* **2024**, *63*, 3955–3961.

[52] Liu, Y.; Wei, J.; Yang, Z. W.; Zheng, L. R.; Zhao, J. K.; Song, Z. M.; Zhou, Y. H.; Cheng, J. J.; Meng, J. Y.; Geng, Z. G. et al. Efficient tandem electroreduction of nitrate into ammonia through coupling Cu

single atoms with adjacent Co_3O_4. *Nat. Commun.* **2024**, *15*, 3619.

[53] Liu, Y. L.; Zheng, Z. Y.; Jabeen, S.; Liu, N. Y.; Liu, Y. X.; Cheng, Y. Y.; Li, Y. X.; Yu, J. W.; Wu, X.; Yan, N. N. et al. Mechanochemical route to fabricate an efficient nitrate reduction electrocatalyst. *Nano Res.* **2024**, *17*, 4889–4897.

[54] Wang, J. J.; Ou, Z. D.; Dong, C. B.; Su, M. Y.; Ali, A.; Kuklin, A. V.; Ågren, H.; Baryshnikov, G. V.; Liu, Y.; Zhao, X. et al. Electronic structure modulated by B-doped Cu promotes electrocatalytic nitrate reduction for ammonia production. *ACS Catal.* **2025**, *15*, 156–166.

[55] Xie, Y.; Cheng, X. J.; Yang, W.; Yan, C. Y.; Wu, S. J. Electrocatalytic reduction of nitrate to ammonia over activated carbon-supported copper-iron bimetallic catalyst synthesized by hydrothermal co-precipitation method. *J. Electroanal. Chem.* **2024**, *972*, 118633.

[56] Zhang, Y. L.; Xiong, J. Q.; Liu, B. P.; Yan, S. H. Electrocatalytic nitrate reduction to ammonia by sea-urchin-like $CoNiO_2$ under mild conditions. *Cell Rep. Phys. Sci.* **2024**, *5*, 101994.

[57] Zou, Y. Y.; Yan, Y. C.; Xue, Q. S.; Zhang, C. Q.; Bao, T.; Zhang, X. C.; Yuan, L.; Qiao, S. C.; Song, L.; Zou, J. et al. MOF-on-MOF heterostructured electrocatalysts for efficient nitrate reduction to ammonia. *Angew. Chem., Int. Ed.* **2024**, *63*, e202409799.

[58] Gong, F.; Hong, S. H.; Song, J. M.; Liu, C. Z.; Liu, S. L.; Feng, J. J.; Wu, Q. W.; Xiong, Y. L.; Medic-Pejic, L.; Cheng, Y. et al. From waste to energy and fuel: Novel Cu_xNi_y/CN catalysts from waste melamine resin for efficient nitrate reduction to ammonia. *J. Mater. Chem. A* **2025**, *13*, 3435–3443.

[59] Li, S. Y.; Yan, J.; Liu, M. H.; Su, H. Localized enriching nitrate/proton on reconstituted Fe nanoparticles boosting electrocatalytic nitrate reduction to ammonia. *J. Energy Chem.* **2025**, *103*, 682–691.

[60] Thani, E. S.; Yang, Y. T.; Du, Q. Y.; Yuan, R.; Zhang, Y. Q.; Yan, Y. T.; Ai, X.; Chen, Y.; Li, S. N. Porous Cu nanosheets for efficient ammonia production via nitrate electroreduction. *Mater. Chem. Front.* **2025**, *9*, 2243–2249.

[61] Wang, J. J.; Liao, K.; Wei, Y. N.; Wang, G. S.; Wan, Z. Y.; Liu, B.; Liu, Z. H.; Deng, X. F.; Zhao, X.; Zhang, H. B. Ru-B modulated electronic structure promotes electrocatalytic nitrate reduction to ammonia and zinc-nitrate battery. *Adv. Funct. Mater.* **2026**, *36*, e16068.

[62] Xin, C. J.; Wei, Y. P.; Bai, J. Q.; Chen, J. S.; Sun, S.; Mao, C. J. Synergistic integration of copper and cobalt-MOF for high-efficiency electrocatalytic nitrate reduction to ammonia. *J. Environ. Chem. Eng.* **2025**, *13*, 115182.

[63] Yang, L. F.; Li, F. Z.; Li, H. X.; Yu, X. B.; Di, Y. Q.; Chen, H.; Xie, S. A.; Xi, X. X.; Han, W.; Yue, X. et al. Facile synthesized Cu_2O nanoparticles for efficient electrocatalytic nitrate reduction to ammonia in ultralow nitrate concentration. *Catal. Sci. Technol.* **2025**, *15*, 4238–4244.

[64] Zhang, D. X.; Liu, Y. H.; Li, D.; Jiang, T. Y.; Chen, Q. T.; Mao, C. L.; Li, L. H.; Jiang, D. L.; Mao, B. D. Carbon dots-boosted active hydrogen for efficient electrocatalytic reduction of nitrate to ammonia. *J. Alloys Compd.* **2025**, *1014*, 178694.

[65] Zhong, W.; Hong, Q. L.; Du, Q. Y.; Xia, B. Y.; Ai, X.; Li, F. M.; Chen, Y. Dual strain regulated RhNiAu trimetallene for efficient plasmonic-promoted acidic nitrate electroreduction. *Energy Environ. Sci.* **2025**, *18*, 4971–4981.